A time-resolved study of PbCl$_2$-induced corrosion of low-alloyed steel in the presence of water vapour at 400 °C

N.B. When citing this work, cite the original published paper.

(article starts on next page)

A time-resolved study of PbCl$_2$-induced corrosion of low-alloyed steel in the presence of water vapour at 400 °C

Hampus Lindmark [*], Torbjörn Jonsson , Jesper Liske

Chalmers University of Technology, SE412 96 Gothenburg, Sweden

ARTICLE INFO

ABSTRACT

A laboratory study of a low-alloyed steel (T22) exposed to an 5% O$_2$ + 20% H$_2$O + N$_2$ bal. gas in the presence of PbCl$_2$(s) and PbO(s) at 400 °C is presented. The presence of PbCl$_2$(s) strongly accelerates corrosion by promoting oxide delamination and crack formation. The corrosion attack is explained according to an electrochemical mechanism, involving the inward diffusion of chlorine ions and formation of metal chlorides at the metal/oxide interface. The role of Cl in PbCl$_2$-indcued corrosion of low-alloyed steels is argued to be the major driving force while the role of Pb in the corrosion attack is minor.

1. Introduction

Replacing fossil fuel with waste in combined heat and power (CHP) plants has gained momentum in the European Union (EU) following more stringent waste management directives and ambitious climate goals [1]. By replacing conventional fossil fuel with waste, a reduction in net CO$_2$ emissions is accomplished while simultaneously reducing the amount of waste in open landfills, which is harmful to both the environment and human health [2]. Furthermore, CHP plants combusting a high fraction of renewable waste fuels combined with bioenergy carbon capture and storage (BECCS) stand out as one of the more promising large-scale carbon-negative techniques, making it interesting for forthcoming developments [3]. However, compared to conventional fossil fuels, combustion of bio-and waste-derived fuels produces a highly corrosive flue gas containing elevated concentrations of alkali chlorides, hydrogen chloride, and heavy metal chlorides [4–6]. Studies have demonstrated that these components can significantly accelerate the corrosion rate of critical boiler equipment, including water walls [6–12] and superheater tubes [13–15]. Consequently, in order to decrease the corrosion rate, the tubes are operated at relatively low steam temperatures, which decrease the electrical efficiency of power plants [16].

Conventional low-alloyed steels are commonly employed for waterwall tubes as they possess good mechanical properties and low cost [17, 18]. However, the low resistance towards corrosion in harsh environments limits its maximum service temperature. Reducing the corrosion rate of the water wall tubes can be accomplished by introducing welded overlay coatings consisting of high-alloyed steels such as Ni-base alloys or austenitic stainless steels. However, the increased expenses for such coatings may outmatch the extended lifespan of the tubes, consequently leading to higher maintenance costs [19,20].

Analysis of deposits collected from heat transfer surfaces in waste-fired boilers utilizing fuel such as recycled waste wood (RWW) and municipal solid waste (MSW) has demonstrated an elevated presence of lead compounds such as lead chloride (PbCl$_2$) compared to fossil fuel-and biomass-fired boilers. These PbCl$_2$-rich deposits, when accumulating on heat exchange surfaces like water walls, may cause severe corrosion [21–23].

The literature on PbCl$_2$-induced corrosion on low-alloyed steels in waste-fired boiler environment is summarized below. Although it is apparent that PbCl$_2$ accelerates corrosion rate of this material type, the underlying mechanism remains elusive.

In 1999, Spiegel presented a melt-driven mechanism to explain the corrosiveness of PbCl$_2$ toward low-alloyed steel [22]. In the cited study, a low-alloyed steel (10CrMo910) was exposed to 15 mg/cm^2 PbCl$_2$ at 500 °C and 600 °C in 5% O$_2$ + He [22]. Since PbCl$_2$ has a melting point of 501 °C [24] the deposited PbCl$_2$ was assumed to be in liquid state. The corrosion morphology after exposure was characterized by a poorly adherent multilayered Fe-rich oxide scale with visible cracks. It was suggested that the PbCl$_2$ melt dissolves the oxide scale under the formation of metal chlorides at the melt/scale interface, and that Fe was transported through the melt as dissolved FeCl$_x$ to the melt/gas interface. At this interface, the higher partial pressure of oxygen (pO$_2$), leads to the oxidation of metal chlorides, the reformation of Fe$_2$O$_3$ and the release of Cl$_2$(g). It was further argued that the released Cl$_2$(g) may act as

a corrosion catalyst re-entering the oxide scale, leading to the re-formation of metal chlorides and the continuation of the oxidation process, a mechanism referred to as "active oxidation", initially proposed by McNallan et al. [25] and further developed by Grabke et al. [26].

Bankiewicz et al., on the other hand, argue that $PbCl_2$ melt is not a prerequisite for accelerated corrosion attack on low-alloyed steel to occur in the presence of $PbCl_2$ [27]. In the referred study, it was shown that a significant corrosion attack was observed at 450 °C, i.e., below the melting point of $PbCl_2$, after 168 h of exposure. The corrosion product was reported to be similar at 450 °C and 550 °C showing a thick multilayered Fe-rich oxide scale with poor adhesion and formation of cracks and voids. Chlorine was detected primarily at the metal/scale interface, presumably in the form of iron chlorides, while Pb was detected further out in association with the iron-rich oxide. Regrettably, the study did not include any scanning electron microscopy (SEM) analysis of the corroded sample exposed to 450 °C, nor did it suggest any corrosion mechanisms [27].

Further strong support for the severe corrosive nature of $PbCl_2$ was presented by Bankiewicz et al. [28] where it was demonstrated that at 400 °C, the mixing of small amounts of $PbCl_2$ in different salts deposited on low-alloyed steel significantly accelerated the corrosion rate of the material, reaching similar corrosion rates as samples exposed solely to $PbCl_2$. The authors concluded that the rapid corrosion of the steel substrate was due to the presence of $PbCl_2$. A mechanism was proposed where the high corrosion rate was attributed to the ability of $PbCl_2$ to react with and destroy the protective chromium oxide (Cr_2O_3), which lead to an accelerated corrosion rate of the steel substrate. However, the suggested mechanism appears to be questionable as the steel compound only contains 2.2 wt% Cr, which is insufficient for the formation of Cr_2O_3 under the referred experimental conditions. A significant increase in the corrosion rate of pure $PbCl_2$ and Pb-containing salts was observed at 500–600 °C, which was attributed to the formation of eutectic melts [28].

In a more recent study by Larsson et al. in humid air at 400 °C, it was demonstrated that the presence of $PbCl_2$ leads to a fast and localized corrosion attack on the low-alloyed steel 10CrMo910 after 24 h of exposure [29]. The author argued that this is due to the rapid decomposition of $PbCl_2$, resulting in the localized release of chlorine species:

$$PbCl_2(s) + H_2O(g) \rightleftharpoons PbO(s) + 2HCl(g)$$
$$\Delta G = +120 kJ \tag{1}$$
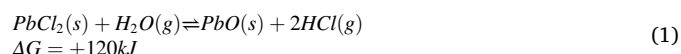
Chloride ions are then suggested to diffuse across the oxide scale to the metal/oxide interface, where high concentrations of metal chlorides were identified. No melt formation was detected, and severe localized spallation of a Fe-rich oxide in the vicinity of the original $PbCl_2$ particles was reported, allowing rapid diffusion of corrosive species to the metal surface [29].

In the reported studies on $PbCl_2$-induced corrosion of low-alloyed steel, the exposure time was fixed, and severe corrosion had already transpired [22,27,29]. The use of a fixed exposure time makes it challenging to study and distinguish the initiating and propagating reaction mechanisms. Given that the initial corrosion process may substantially impact the corrosion behavior in later stages, improving knowledge of the initial corrosion mechanisms is important for furthering our understanding of $PbCl_2$-induced corrosion. Furthermore, previous studies have fully attributed the propagating corrosion mechanisms to Cl-induced corrosion and the formation of metal chlorides, either by melt formation or rapid release of Cl from the decomposition of $PbCl_2$. While it has been reported that Pb in $PbCl_2$ plays an important role in the corrosion attack of Cr-containing alloys by reacting with the protective chromia layer [22,27,30], its influence on low-alloyed steel has not been studied at length. This understanding is of importance to further develop corrosion-preventing strategies and improve our knowledge of the rapid degradation rates observed in water wall tubes of waste-fired boilers.

The aim of this work is to improve the knowledge of the corrosion

mechanism of $PbCl_2$-induced corrosion on low-alloyed steel (10CrMo910) and elaborate on the role of both Pb and Cl. A well-controlled laboratory study was carried out where the samples were exposed isothermally with a continuous gas flow containing 5% O_2 + 20% H_2O + N_2 bal. at 400 ± 2 °C. To monitor the temporal evolution of corrosion, a time-resolved study was conducted with a maximal exposure time of 168 h. Prior to exposure, the samples were deposited with 0.185 mg/cm² $PbCl_2$ or left without any deposition (reference sample). In addition, samples deposited with 0.185 mg/cm² PbO were prepared in response to the findings from the $PbCl_2$-deposited samples (Section 4.2). The morphology and microstructure of the corrosion products were analyzed using X-ray diffraction (XRD) and scanning electron microscopy (SEM) coupled with an energy-dispersive X-ray (EDX) detector.

2. Experimental

2.1. Sample preparation

The alloy studied was a low-alloyed steel, Fe-2.25Cr-1Mo (also referred as 10CrMo910 or T22), with the following nominal chemical composition, expressed in wt% and at%:Table 1).

Before exposure, the samples were cut into 15 × 15 × 2 mm coupons, and the surface edges were mechanically ground in water using silicon carbide paper with a grit size of 1000. Subsequently, the samples were automatically ground in water using a Struers TegraPol-31 polishing instrument with a grit size of 320 and polished with three diamond suspensions 9, 1 and 0.5 μm until a mirror-like appearance was achieved. The samples were then degreased and washed by immersing the samples in acetone during ultrasonic agitation for 15 min. $PbCl_2$ was applied to the samples by spraying a $PbCl_2$ di ionized-water solution on the sample for a total of 0.185 mg/cm² while continuously drying the sample to ensure fast solvent evaporation.

2.2. Exposure

A schematic of the isothermal experimental setup is shown in Fig. 1. The exposures were carried out isothermally at 400 ± 2 °C using a horizontal silica tube of 80 mm in diameter. The samples were subjected to a continuous gas flow containing 5% O_2 + 20% H_2O + N_2 bal. with a flow rate of 3 cm/s. The samples were positioned on an alumina sample holder parallel to the gas flow. The exposures were carried out for 1, 24 and 168 h separately, and a total of three samples were exposed simultaneously. The gas flow was measured using a MesaLabs Bios DryCal Definer 220 calibrator. The H_2O content in the gas was achieved by coupling a water bath, set to 60 °C, to the system, where water vapor was added to the gas via a Nafion membrane. The water vapor content was measured at the exit of the membrane just before the entrance to the horizontal tube furnace using a Mitchell instruments Optidew Vision™ chilled mirror humidity sensor. Following the exposure, the samples were placed inside a desiccator, with SICAPENT® (P_2O_5) employed as the desiccating agent.

The samples were subjected to broad ion beam (BIB) milling after exposure to attain high-quality cross-sections. Prior to the milling process, a thin silica wafer was glued on top of the exposed samples and allowed to dry overnight. The sample was then cut in half and polished to a 0.5 μm surface finish using a Lecia EM TXP instrument operating at low speed and without lubricant. The samples were thereafter ion beam milled for 6 h using a Lecia TIC 3x instrument with triple Ar-ion guns

Table 1
Nominal composition (wt% and at%) of T22.

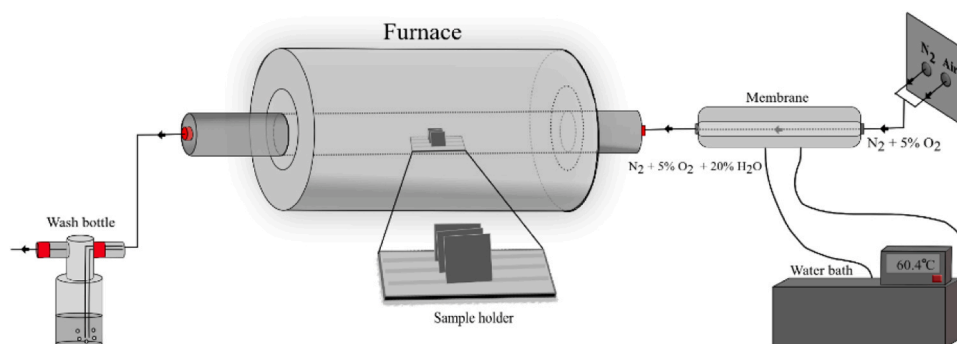| Alloy	Fe	Cr	Mo	Si	Mn	C	P	S
T22 (wt%)	96	2.2	0.9	0.3	0.5	0.08	0.01	0.01
T22 (at%)	95.78	2.47	0.51	0.59	0.45	0.11	0.02	0.02

Fig. 1. Schematic of the furnace setup.

operating at 8 kV.

3. Analytical techniques

The surfaces and resulting cross-sections of the exposed samples were analyzed using an FEI QUANTA ESEM 200 scanning electron microscope (SEM) operated in high vacuum mode. Backscattering electron (BSE) mode was utilized for imaging with an accelerated operating voltage ranging from 10–20 kV. Chemical elemental analysis was carried out using an Oxford Instruments X-MaxN 80 T EDX coupled to the SEM instrument and operated at 20 kV. The crystalline phases of the oxide scale were characterized using X-ray diffraction (XRD). The XRD analysis was performed on a Siemens Bruker 8 Discovery diffractometer equipped with a Cu source and with a measuring range of $10 < 2\Theta < 90°$.

Oxide thickness measurements were carried out by combining SEM imaging with a vector graphic editor software (INKSCAPE). In total, four SEM BSE images were acquired within the prepared BIB cross-sectional area and combined in a panoramic fashion. Subsequently, the images were subjected to analysis with INKSCAPE, and the oxide thickness was measured by drawing vertical lines over the oxide scale, which each pixel converted to micrometers. A total of 9 measuring points were taken for each sample, and the average oxide thickness and standard deviation were recorded. A total of two samples for each exposure type were analyzed.

4. Results

4.1. Oxide growth rate

Fig. 2 shows the average oxide thickness for T22 exposed to 1, 24 and 168 h in 5% O_2 + 20% H_2O + $PbCl_2$, 5% O_2 + 20% H_2O + PbO and 5% O_2 + 20% H_2O, respectively. In all cases, the samples show parabolic kinetics, indicating that oxide growth is diffusion-controlled. However, in the case of the $PbCl_2$ exposed samples, a significant spread in oxide thickness was observed, making the parabolic kinetic less apparent.

After 1 h of exposure in the presence of $PbCl_2$, the oxide thickness was approximately 4 μm, a value roughly 40 times greater than the corresponding value for the reference samples and the samples exposed to PbO. The oxide thickness continued to increase over time, reaching about 6 μm and 15 μm after 24 and 168 h of exposure, respectively.

The samples exposed to PbO obtained a significantly thinner oxide compared to the $PbCl_2$ samples. The oxide thickness remained comparable with the samples exposed without any deposit after 24 h of exposure and was measured to about 0.1 and 0.6 μm after 1 h and 24 h of exposure, respectively. However, after 168 h, a notably lower oxide thickness was measured for the sample exposed to PbO, measuring roughly half the oxide thickness of the reference samples (0.8 and 1.8 μm, respectively). Regardless of exposure time, the samples exposed to PbO and without deposit exhibited a homogenous oxide scale, as
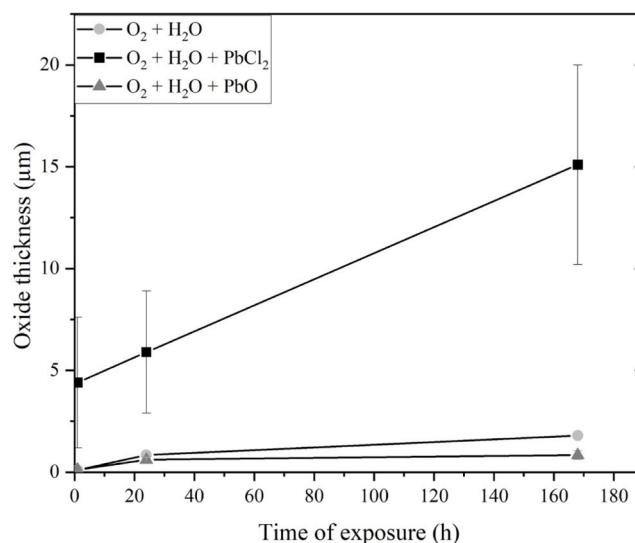

Fig. 2. Average oxide thickness of T22 exposed for 1, 24 and 168 h at 400 °C in O_2 + H_2O + $PbCl_2$, O_2 + H_2O + PbO, and O_2 + H_2O.

indicated by the lack of error bars for these data points.

4.2. Oxide morphology

4.2.1. O_2 + H_2O + $PbCl_2$

Fig. 3 shows plan view SEM images of samples exposed in the presence of $PbCl_2$ after 0, 1, 24 and 168 h. The $PbCl_2$-exposed samples after 1 h is characterized by a heterogeneous surface with two typical features: large Fe-rich oxide nodules growing in close vicinity to the original $PbCl_2$ particles (bright areas in the SEM images) and a relatively homogenous Fe-rich oxide detected in regions with small amount of deposited $PbCl_2$, referred to as "base oxide" (Fig. 3b). The base oxide was smooth with needle-shaped hematite whiskers growing on top of the surface (see highlighted area in Fig. 3b). In addition, XRD analysis revealed that the original $PbCl_2$ particles on the surface had converted to Mendipite $Pb_3Cl_2O_2(s)$, an oxyhalide of lead after 1 h of exposure (Fig. 4). After 24 h of exposure, a considerable amount of the original $PbCl_2$ particles were overgrown (Fig. 3c). XRD showed that Mendipite was no longer present on the surface, and instead, intense peaks corresponding to PbO (Litharge) were detected (Fig. 4). This was also confirmed by EDX analysis, where no Cl was detected at the bright Pb-containing areas. After 168 h of exposure, similar features were apparent as after 1 and 24 h of exposure, namely, the sample surface exhibited two regions: partly or completely overgrown original $PbCl_2$ particles and areas with base oxide having hematite needle-shaped whiskers growing on top (Fig. 3d-e). XRD analysis of the samples
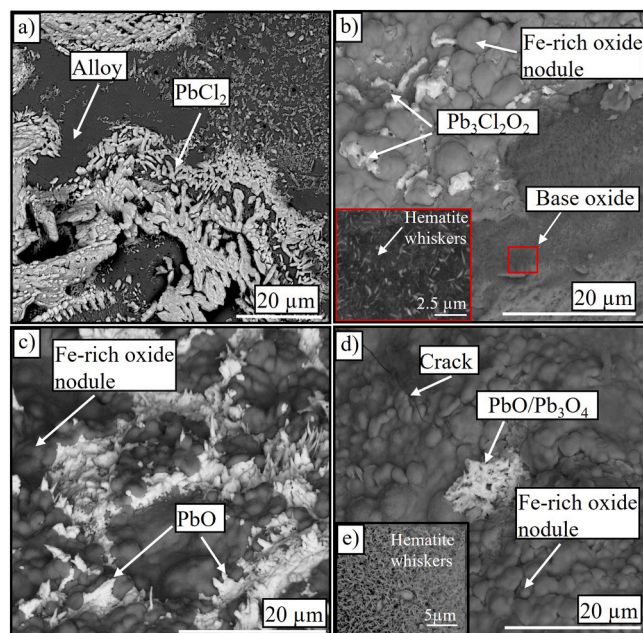
Fig. 3. SEM-BSE plan view SEM images of T22 exposed to 5% O_2 + 20% H_2O +N_2 bal. + $PbCl_2$ at 400 °C for a) 0 h, b) 1 h, c) 24 h, d) 168 h, e) hematite whiskers observed on the sample after 168 h of exposure.
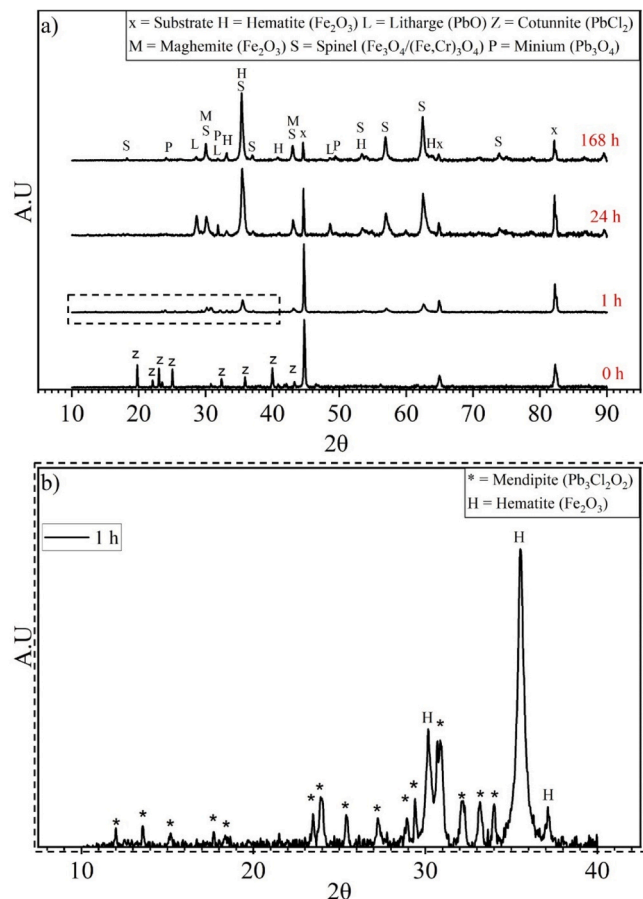

Fig. 4.. a) XRD spectra of T22 exposed to 5% O_2 + 20% H_2O +N_2 bal. + $PbCl_2$ at 400 °C for 0 h, 1 h, 24 h and 168 h, b) XRD spectra of highlighted area in (a).

exposed for 168 h revealed that Pb_3O_4 had formed which is believed to originate from further oxidation of PbO on the scale surface (Fig. 4). Visible cracks were observed on the sample's surface after 168 h of exposure. However, they may have developed post-exposure during cooling of the sample.

4.2.2. O_2 + H_2O + PbO

The XRD analysis of the T22 alloy exposed to $PbCl_2$ revealed that within 24 h of exposure, the original $PbCl_2$ particles had converted entirely to PbO. As such, to gain insights into the propagating mechanism of $PbCl_2$-induced corrosion, it becomes crucial to explore the impact of PbO formation. To isolate the effect of PbO, T22 samples deposited with PbO were prepared and exposed under identical experimental conditions as the $PbCl_2$ samples as described in Section 2.2.

Fig. 5 shows plan view SEM images of the PbO-exposed samples after 0, 1, 24 and 168 h. When comparing the distribution of PbO particles with $PbCl_2$ before exposure, it may be noted that the deposited PbO exhibited two characteristics: small sheet-like PbO agglomerates and well-dispersed PbO particles that were seen across the entire sample, creating a more even coverage compared to $PbCl_2$ (Fig. 5a).

After 1 h of exposure, the PbO particles and PbO sheets were still present on the sample surface (Fig. 5b). There was no indication of accelerated corrosion in the vicinity of the PbO particles. After 24 h of exposure, two distinct features were observed on the surface: deposited PbO particles and a Fe-rich oxide containing traces of Pb (Fe-Pb-O) (Fig. 5c). The oxide scale remained homogenous throughout the sample, and there was no indication of spallation or crack formation.

After 168 h of exposure, similar morphology was observed as after 24 h, namely a homogenous and consistent Fe-Pb-O oxide with visible PbO particles (Fig. 5d). The XRD analysis after 168 h of exposure indicate the possible formation of Magnetoplumbite ($PbFe_{12}O_{19}$) (Fig. 6). In addition, both PbO and Pb_3O_4, were identified by XRD. Pb_3O_4 is believed to originate from oxidation of PbO. Lastly, in comparison to the $PbCl_2$ exposed samples, no hematite whiskers were observed on the surface of samples exposed to PbO. This is consistent with the XRD analysis shown in Fig. 6 where no hematite was detected regardless of exposure time.
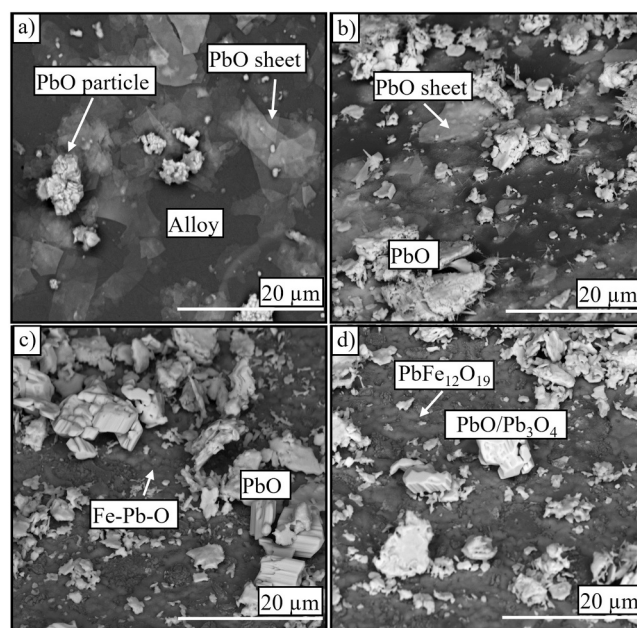

Fig. 5. SEM-BSE plan view images of T22 exposed to 5% O_2 + 20% H_2O +N_2 bal. + PbO at 400 °C for a) 0 h b) 1 h, c) 24 h and d) 168 h.
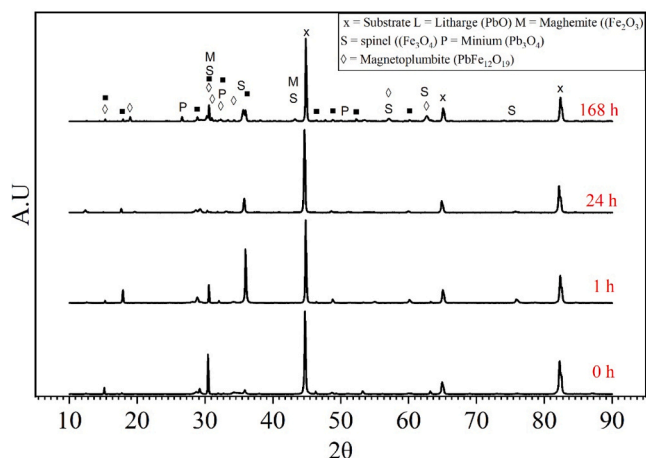
Fig. 6. XRD spectra of T22 exposed to 5% O_2 + 20% H_2O + N_2 bal. + PbO at 400 °C for 0 h, 1 h, 24 h and 168 h.

4.3. Oxide microstructure

4.3.1. $O_2 + H_2O + PbCl_2$

Key features from the cross-section analysis of a sample exposed to $PbCl_2$ after 1 h of exposure are shown in Fig. 7. The oxide scale is interpreted to consist of an outward-growing hematite and magnetite Fe_2O_3/Fe_3O_4 and a porous inward-growing chromium containing spinel $(Fe,Cr)_3O_4$ (Fig. 7b). The interface between the inward and outward-growing oxide was determined based on the presence of Cr from EDX point analysis. The oxide thickness throughout the cross-section varied between 2–6 μm, where the greatest thickness was observed in close proximity to the original $PbCl_2$ particles. In addition, these areas were associated with frequent spallation of the oxide scale and crack formation. However, even further away from the regions with high concentrations of original $PbCl_2$ particles, traces of void formation in the oxide could be found (Fig. 7b). Furthermore, the EDX map revealed Cl-containing compounds in two regions, namely on top of the oxide scale in correlation to Pb corresponding to Mendipite and at the vicinity of the metal/oxide interface, presumably in the form of iron chloride ($FeCl_2$) (Fig. 7c).

After 24 h of exposure, severe delamination and void formation was observed in close vicinity to the original $PbCl_2$ particles (Fig. 8). The scale consisted of delaminated multilayered outward growing Fe-rich

oxides and an inward-growing $(Fe,Cr)_3O_4$. In addition, a roughly 0.5 μm bright contrast Fe-Pb-O oxide layer was observed on top the outward-growing hematite/magnetite layer (Fig. 8b). The Fe-Pb-O feature was rather unevenly distributed over the surface and observed in the vicinity of the original $PbCl_2$ particles. According to EDX analysis, the Fe-Pb-O regions contained approximately 3 at% Pb. EDX map analysis revealed that Mendipite was no longer present on the oxide surface, as there was no longer any correlation between Pb and Cl (Fig. 8c). This agrees with the findings from the XRD analysis presented in the previous section. A high concentration of Cl was found close to the metal/oxide interface as with the sample exposed to 1 h, likely indicating the presence of $FeCl_2$.

After 168 h of exposure, the oxide scale thickness remained heterogeneous, with increased thickness near the original $PbCl_2$ particles (Fig. 9). The oxide scale was porous, being characterized by cracks, delamination, and voids. Severe scale spallation was observed for the oxide growing inside previous voids (Fig. 9b). The bright areas in the BSE images consisted of both PbO and Pb_3O_4 suggested by the XRD analysis (Fig. 9b). In addition, similar to the samples exposed for 24 h, a roughly 1–2 μm Fe-Pb-O oxide was observed at the oxide/air interface in the vicinity of the original $PbCl_2$ particles. This oxide phase was not present continuously through the oxide scale. Below, an outward-growing oxide was observed that was concluded to consist of hematite and magnetite based on EDX and XRD results. The inward-growing oxide consisted of $(Fe,Cr)_3O_4$ spinel. The bright spots observed in the inward-growing oxide consisted of Mo precipitates. Lastly, the EDX maps revealed high concentrations of Cl at the metal/oxide interface (Fig. 9c).

4.3.2. $O_2 + H_2O + PbO$

After 1 h of exposure, both the reference sample and the sample exposed to PbO had formed an oxide layer with a thickness of < 0.1 μm, which was barely visible using the current SEM set-up. Consequently, these samples will not be presented in detail in this paper.

Fig. 10c and d shows SEM cross-section images of the samples exposed to PbO after 24 and 168 h. After 24 h, the oxide scale was 0.6 μm thick and strongly adherent to the alloy substrate, (Fig. 10c). Due to the relatively thin oxide, no comprehensive EDX analysis was carried out on this sample. However, based on the different contrast throughout the cross-section and results from the plan view analysis, it is suggested that the oxide was multilayered, consisting of an outward-growing oxide scale comprised of a Pb containing Fe-oxide (Fe-Pb-O) at the top layer and a Fe-rich oxide in the middle. A darker region was observed at the
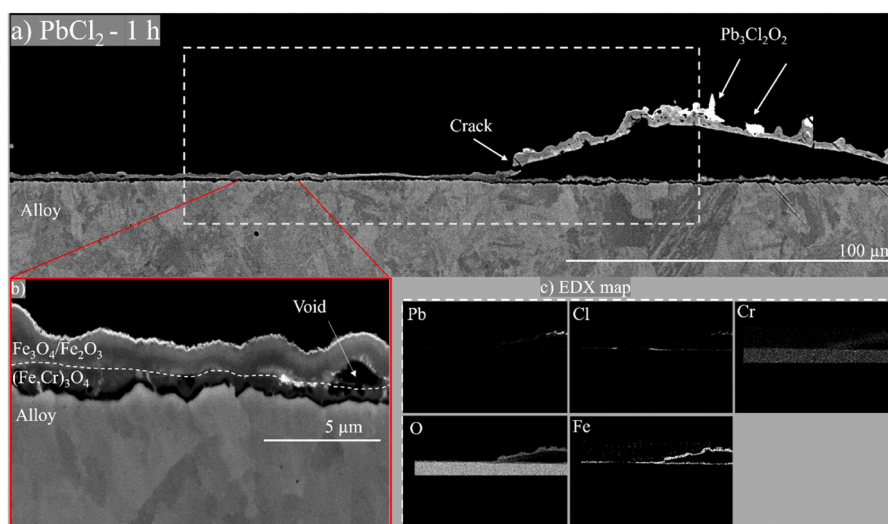

Fig. 7. a) BIB SEM-BSE cross-section images of T22 exposed at 400 °C in 5% O_2 + 20% H_2O + N_2 bal. + $PbCl_2$ for 1 h, b) higher magnification of selected area in (a), c) EDX mapping of highlighted area in (a).

Fig. 8. a) BIB SEM-BSE cross-section images of T22 exposed at 400 °C in 5% O_2 + 20% H_2O +N_2 bal. + $PbCl_2$ for 24 h, b) higher magnification of selected dense area, c) EDX mapping of highlighted area in (a).
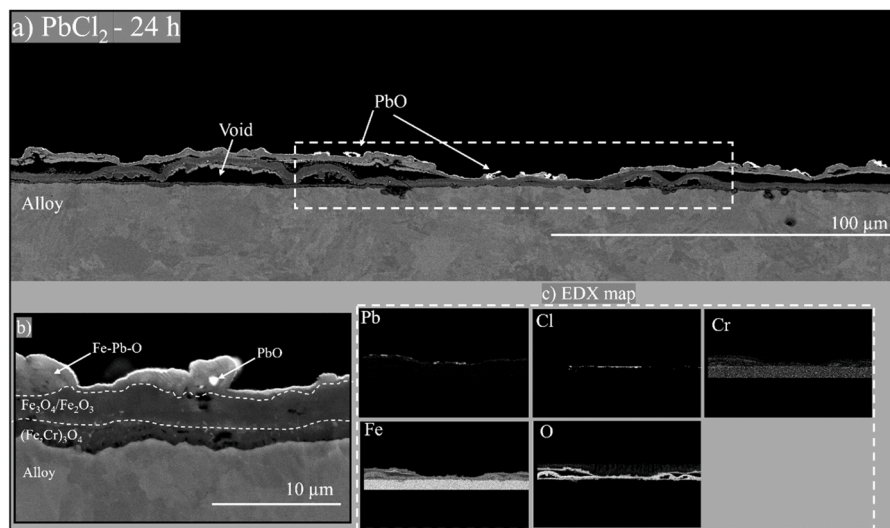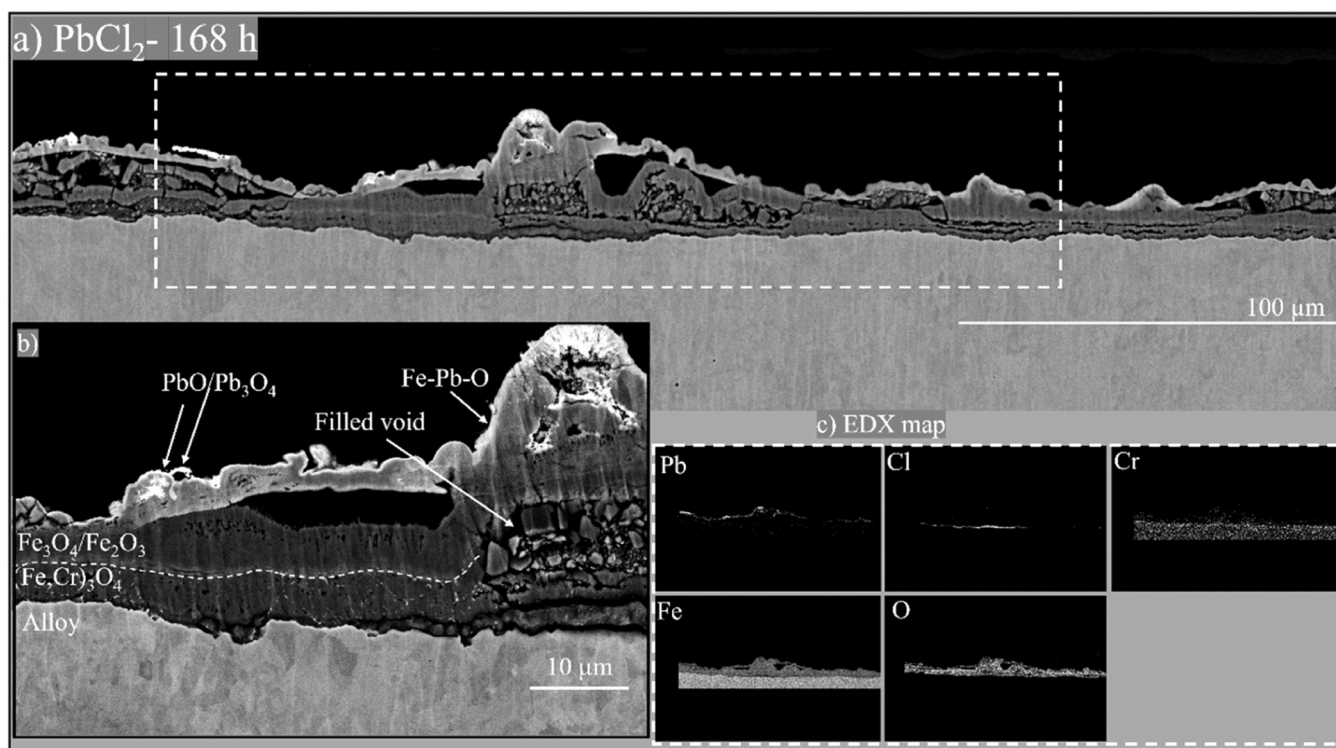

Fig. 9. a) BIB SEM-BSE cross-section images of T22 exposed at 400 °C in 5% O_2 + 20% H_2O +N_2 bal. + $PbCl_2$ for 24 h, b) higher magnification of selected area in (a), c) EDX mapping of highlighted area in (a).

interface between the metal and the oxide layer, indicating the formation of an inward-growing $(Fe,Cr)_3O_4$ oxide (Fig. 10c).

A similar oxide morphology was observed after 168 h (Fig. 10d), with the oxide scale having grown to about 0.8–1 μm. EDX analysis revealed that the bright top layer consisted of about 3 at% of Pb and further XRD analysis concluded that Magnetoplumbite ($PbFe_{12}O_{19}$) was present on the surface (Fig. 6). Bright spherical-shaped features were detected in the Magnetoplumbite containing an elevated concentration of Pb according to EDX point analysis. Below, a Fe_3O_4 oxide layer was present, and at the metal oxide interface, a rather porous inward-growing oxide was observed, suggested to be a spinel $(Fe,Cr)_3O_4$

based on XRD data. Similar to the sample exposed to 24 h, there were no signs of spallation or formation of cracks along the oxide scale.

4.3.3. O_2 + H_2O (reference)

After 24 and 168 h of exposure, the reference samples had formed an adherent uniform oxide scale with a thickness of about 0.9 and 1.4 μm, respectively (Fig. 10a, b). The oxide scale was multilayered with hematite whiskers growing on top of an outward-growing (Fe_3O_4) magnetite and a thinner inward-growing $(Fe,Cr)_3O_4$ spinel at the metal/oxide interface.
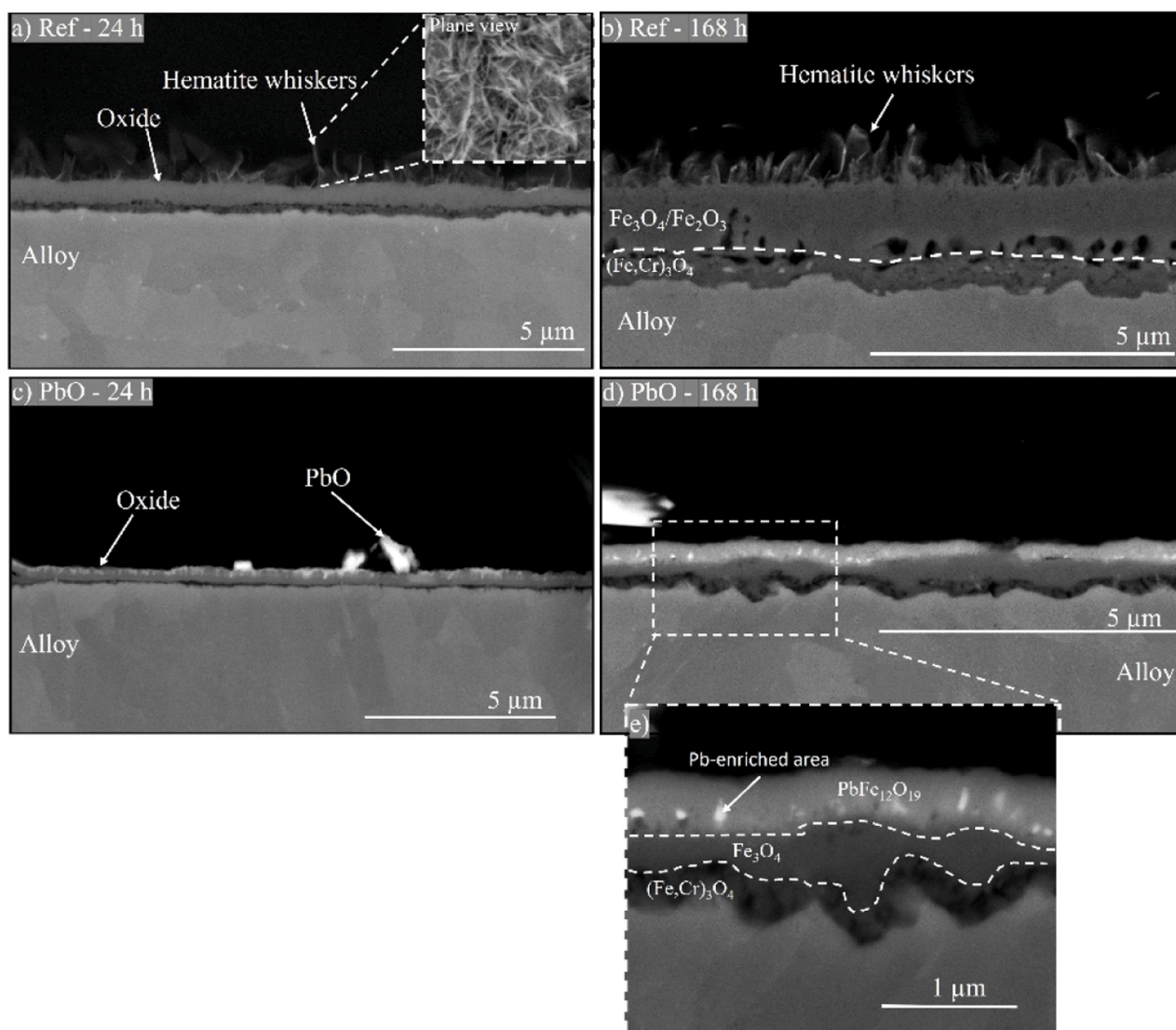
Fig. 10. BIB SEM-BSE cross-section images of T22 exposed at 400 °C. a) 5% O_2 + 20% H_2O + N_2 bal. after 24 h, b) 5% O_2 + 20% H_2O + N_2 bal. after 168 h, c) 5% O_2 + 20% H_2O + N_2 bal. + PbO after 24 h, d) 5% O_2 + 20% H_2O + N_2 bal. + PbO after 168 h, e) higher magnification image of the area highlighted in (d).

5. Discussion

5.1. Oxidation of T22 in the absence of salt (reference)

All exposures carried out on T22 in the absence of salt resulted in a slow-growing oxide exhibiting both similar thickness and microstructure as reported in previous studies carried out on the same alloy type in humidified air [31–33]. Accordingly, the microstructure analysis revealed that the oxide scale remained uniform and with no indication of spallation or crack formations regardless of exposure time. After 168 h, the oxide scale consisted of an inward growing spinel $(Fe,Cr)_3O_4$ and an outward growing bi-layered Fe-rich oxide. Based on [31] and the analysis performed in this paper, the outward growing oxide is interpreted to consist of hematite (Fe_2O_3) at the scale/gas interface and a magnetite (Fe_3O_4) growing beneath the hematite layer. This is further argued by observing the features shown at the oxide/air interface represented by the highlighted area in Fig. 10a were the formation of needle shaped whiskers on the surface was observed. These features have been observed in previous studies upon exposing low-alloyed steels and pure iron in the presence of water vapor in relevant temperatures and is reported to primarily consist of hematite [34,35]. The interpretation of the microstructure where an outward and inward growing oxide layers are

separated, is based on the relatively slow diffusion of Cr^{3+} in spinel oxides compared to Fe^{2+}/Fe^{3+} [36,37]. Consequently, the rapid outward diffusion of Fe ions facilitates the formation of an outward growing Fe-oxide layer, while Cr is relatively immobile within the inward growing spinel oxide.

T22 exposed in a O_2 + H_2O environment at 400 °C in the absence of salt have the ability to form a protective oxide scale. Furthermore, the oxidation process is clearly diffusion controlled and as indicated by Fig. 2, the growth rate of the scale decreases with time.
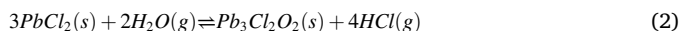
5.2. The corrosivity of $PbCl_2$

The experiment shows that small amounts of $PbCl_2$ greatly accelerates the corrosion rate of T22 exposed at 400 °C in a O_2 + H_2O environment. Already after one hour a roughly 4 μm thick oxide scale has formed (Fig. 2). Thus, the $PbCl_2$ exposed samples exhibit 3-4 times thicker oxide scale after 1 h of exposure compared to the corresponding reference samples after 168 h (Fig. 2). Corrosion was especially rapid in the vicinity of $PbCl_2$ particles. In areas near large $PbCl_2$ particles, the oxide thickness was up to twice as thick as areas more distant from $PbCl_2$ particles. Still, these regions suffered from rapid corrosion, with the oxide scale being about 20 times thicker compared to the reference

samples after 1 h.

5.2.1. The role of Cl

Cross-section analysis showed that chlorine was accumulated in the metal/oxide interface and in association with Fe already after 1 h of exposure. As Pb was absent in this area according to EDX analysis (Fig. 7c), Cl must have migrated from the PbCl$_2$ particle. XRD analysis, revealed that Mendipite (Pb$_3$Cl$_2$O$_2$) were present on the oxide surface after 1 h of exposure (Fig. 4). The occurrence of Mendipite on the top of the oxide scale at this early stage highlights the reactivity of PbCl$_2$ in this environment. After 24 h of exposure, the Mendipite particles had in turn reacted to form PbO. Based on these observations, it is proposed that chlorine is released from PbCl$_2$ in a two-step process, resulting in the formation of HCl(g) at the surface of the sample:

$$3PbCl_2(s) + 2H_2O(g) \rightleftharpoons Pb_3Cl_2O_2(s) + 4HCl(g) \qquad (2)$$

$$Pb_3Cl_2O_2(s) + H_2O(g) \rightleftharpoons 3PbO(s) + 2HCl(g) \qquad (3)$$

The release of chlorine from PbCl$_2$ may also occur in dry air, leading to the formation Mendipite and Cl$_2$(g). Many studies have demonstrated that chlorine containing compounds, e.g., HCl(g), accelerate the corrosion of various steel types in an oxidizing environment at high temperatures [22,26,28,29,38–40]. The acceleration of corrosion by chlorine-containing compounds has been suggested to occur according to the "active oxidation" mechanism where the diffusion of Cl$_2$(g) and gaseous metal chlorides through the oxide scale in cyclic manner play an important part [26]. This mechanism is initiated by the oxidation of HCl (g) to form Cl$_2$(g) and H$_2$O(g), (i.e the Deacon reaction):

$$4HCl(g) + O_2(g) \rightleftharpoons 2Cl_2(g) + 2H_2O(g) \qquad (4)$$
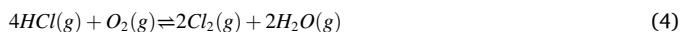
Cl$_2$(g) is argued to diffuse through the oxide scale as gas molecules via cracks and pores, until it reaches and reacts with the metal substrate, forming metal chlorides MeCl$_x$(s/g). The high vapor pressure of metal chlorides allows rapid diffusion of gaseous metal chlorides towards the oxide/gas interface. The gaseous metal chlorides will eventually reach a region of sufficiently high pO$_2$ to form corresponding metal oxides, resulting in the formation of a porous, poorly adherent oxide and the release of Cl$_2$(g). Cl$_2$(g) then re-enters the oxide scale and repeats the steps described above, acting as a corrosion catalyst [26].

A notable challenge with the "active oxidation" mechanism is that it postulates the gaseous transport of Cl$_2$(g) and MeCl$_x$(g) through the scale, while disallowing gaseous transport of O$_2$(g) through the same scale. The latter is a prerequisite in order to keep the oxygen gradient across the scale and consequently, to enable the transport of gaseous chlorine species through the scale without being oxidized. Since gas diffusion through an oxide scale requires the presence of cracks and/or connected voids, we first need to address the size of a crack. A crack within the oxide microstructure would be ranging from nanometer range when two separate surfaces has formed to several micrometers in width, see e.g., the crack in Fig. 7. Since the sizes of the gaseous molecules in question is in the sub-nanometer range, even the initial crack stage will easily fit all molecules. Consequently, the gas diffusion rate through a crack is primarily determined by the concentration gradient and the molecular weight (according to Graham's law), given that other parameters such as e.g., temperature and pressure is fixed. From both these parameters, the diffusion of O$_2$(g) molecules should be fastest. The molar mass of the O$_2$(g) molecule is only 32 g/mol, compared to Cl$_2$(g) (70.9 g/mol) and FeCl$_2$(g) (126.8 g/mol). Furthermore, the concentration gradient points in the favor of O$_2$(g) having the fastest diffusion. In many systems, the partial pressure of O$_2$(g) in the gas atmosphere is in the %-levels, typically 5–10% in a combustion environment [4]. The partial pressure of Cl$_2$(g) is only in the ppb-range, for the same environment. This since the presence of water vapor, typically 10–20%, shifts the equilibrium of reaction (4) to the left [41]. Nevertheless, the mechanism stipulates that the oxidation of the gaseous metal chlorides is converted into their corresponding oxides subsequent to their diffusion

through the oxide scale, reaching higher partial pressure of oxygen. The Cl$_2$(g) formed from the resulting reaction is then suggested to repeat this cycle by inward gas diffusion through the scale, where O$_2$(g) still being disallowed to do the same. To summarize, this mechanism requires that the oxide scale allows the passage of gaseous Cl$_2$ and MeCl$_x$ molecules through the oxide scale while the gas diffusion of O$_2$ is limited.

In light of this, Folkeson et al. [42] proposed an electrochemical approach to elucidate the diffusion of chlorine in high-temperature corrosion. In the paper referred to, the stainless steel AISI310 was exposed to 500 ppm HCl(g) in dry O$_2$ conditions. In the "electrochemical mechanism", HCl(g) is proposed to deprotonate cathodically on the oxide surface, forming Cl$^-$ ions that diffuses inwardly via oxide grain boundaries according to:

$$\frac{1}{4}O_2(g) + HCl(g) + e^- \rightleftharpoons \frac{1}{2}H_2O(g) + Cl^-(ads) \qquad (5)$$
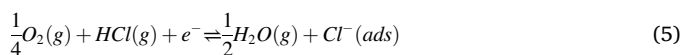
The corrosion acceleration induced by HCl was, according to the authors, due to the formation of FeCl$_2$ that promotes an increased ion flux through the scale, as metal chlorides are expected to decorate the oxide grain boundaries that is argued to promote improved diffusion of corrosive species. In addition, the authors also stipulates that the location of metal chlorides may exist at several locations in the oxide scale, depending on the rate of the inward and outward diffusion of chlorine and metal ions, respectively. In a more recent paper, the corrosion acceleration of KCl(s) on the low-alloyed steel T22 was explained primarily by extensive crack formation and delamination of the oxide scale, leading to the formation of a multilayered scale [31]. Even though traces of metal chlorides were detected on the corroded sample, the authors could not determine if the cracks and delamination was due to the formation of metal chlorides or other aspects (such as e.g., the influence of K). However, a corrosion morphology showing delamination and/or cracks, when steels been exposed towards chlorine containing compounds have often been reported [17,41,43].

According to the SEM/EDX analysis in this study, Cl-containing compounds were detected at the metal/oxide interface (Figs. 7–9), presumable in the form of iron chloride (FeCl$_2$). The stability of metal chlorides at a fixed temperature and pressure is correlated to the partial pressure of oxygen and chlorine. From the thermodynamic stability diagram calculated with Factsage 7.3 (Fact Pure Substance Database, FactPS) shown in Fig. 11 it is evident that iron chlorides are stable at low partial pressures of oxygen, i.e., at the metal/oxide interface. Furthermore, from these diagrams, it is argued that FeCl$_2$(s) is the stable metal chloride that has formed in this study. The observation of FeCl$_2$ at the metal/oxide interface are in accordance with previous studies on chlorine induced corrosion on low-alloyed steel [22,38,44].
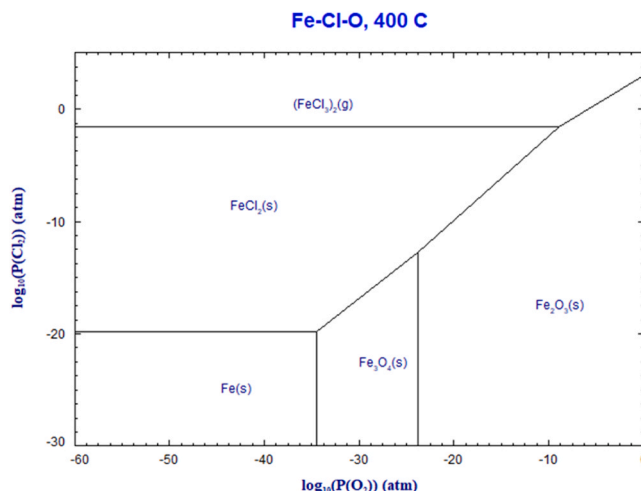

Fig. 11. Thermodynamic stability diagram of the Fe-Cl-O system at 400 °C.

Furthermore, the results from this study showed that the area close to the $PbCl_2$ particles have undergone substantial delamination as well as cracking of the oxide scale (Figs. 7–9). Further away from the original $PbCl_2$ particles, only minor spallation and void formation was observed. It has been argued in previous studies that the formation of $FeCl_2$ at the metal/oxide interface increases the corrosion attack on various steel substrates, including low-alloyed steels, by reducing the adhesion of the oxide scale leading to severe delamination of the oxide scale [34]. The substantial spallation observed in the vicinity of original $PbCl_2$ particles could be attributed to the expected high concentration of metal chlorides formed by the local release of HCl(g) described in Eqs. (2) and (3).

In light of this, a corrosion mechanism and the growth process of the oxide scale formed in presence of $PbCl_2$ is proposed and illustrated in Fig. 12. In the first step, it is argued that the release of HCl(g) from Eqs. (2) and (3), is converted to chlorine ions, according to Eq. (5), and diffuse inwardly through the oxide scales. By deploying a transport mechanism based on ions, rather than gaseous species, it is argued that the inward diffusion of the monovalent Cl^- is expected to be faster than the divalent O^{2-}. The faster ion diffusion of Cl^- compared to O^{2-} would lead to an accumulation of $FeCl_2(s)$ at the metal/oxide interface, which was confirmed during SEM cross section analysis. The high concentration of metal chlorides accumulated at the metal/oxide interface is suggested to facilitate spallation of the oxide scale as the adherence between the metal and the oxide scale is argued to decrease by the presence of $FeCl_2$. Furthermore, the oxide scale is not completely detached from the metal, and it may continue to grow somewhat after delamination. In addition, $FeCl_2$ may evaporate (the equilibrium pressure of $FeCl_2(g)$ is $4.16 * 10^{-7}$ atm at 400 °C, calculated using FactSage 7.3 FactPS database). Once the oxide scale becomes detached, its continued growth and the vapor pressure of $FeCl_2$ introduces stresses and causes buckling and subsequently cracking of the scale. Once cracked, O_2 and H_2O may diffuse to the metal/oxide interface, resulting in rapid oxidation kinetics and the formation of a new oxide scale. As

Fig. 12. Proposed corrosion mechanism. (1) $PbCl_2(s)$ reacts with the surrounding water vapor forming, $Pb_3Cl_2O_2(s)$ while simultaneously releasing HCl (g). HCl(g) is suggested to adsorb onto the oxide surface and undergo deprotonation, producing Cl ions according to Folkeson et. al [42]. (2) Cl ions diffuse through the oxide scale, resulting in the formation of $FeCl_2(s/g)$ at the metal/oxide interface. (3) The formation of $FeCl_2$ promotes delamination and buckling of the oxide scale, leading to crack formation, which facilitates rapid diffusion of oxidizing species to the metal/oxide interface. (4) This process leads to the formation of a new oxide scale beneath the initial one. (5) It is suggested that a similar oxide growth mechanism continuous throughout the exposure, resulting in the formation of several delaminated oxide scales with poor protective properties.

$FeCl_2$ remained present after 24 and 168 h of exposure at the metal/oxide interface, and the formation of multilayered oxide scales were observed it is argued the corrosion attack is primarily driven by a repeating crack-induced procedure, constantly forming new oxide layers as the gas environment get direct access to the metal surface through the formed cracks. This type of crack-induced corrosion mechanism was recently published for T22 when exposed to KCl(s) at 400 °C [31].

Further away from the $PbCl_2$ particles, the oxide scale was well adherent and showed less signs of void formation (Fig. 8b). Instead, the corrosion attack is clearly diffusion controlled. However, even though these areas are located away from $PbCl_2$ particles, the corrosion rate is considerably higher compared to the corresponding reference exposure without salt. Thus, the suggested crack-induced corrosion mechanism does not account for the observed increase in oxide thickness. The dense oxide scale reinforces the argument that the active oxidation mechanisms cannot account for the increased oxide thickness in these regions as this mechanism is dependent on the formation of a porous oxide scale for the transportation of $Cl_2(g)$ to the metal surface. Instead, it has been suggested in previous studies that an increase in corrosion rate on low-alloyed steel in the presence of alkali chlorides is facilitated by the formation and decoration of metal chlorides in the grain boundaries of the oxide scale that enhance outward and inward transport of iron and oxygen ions, respectively [32,42]. However, in this study, the relatively thin oxide scales together with the limit resolution of the SEM analysis made it challenging to study this effect in depth for $PbCl_2$.

5.2.2. The role of Pb

While Cl in $PbCl_2$ is argued to contribute to a significant increase of the corrosion rate on T22 according to the proposed mechanism described in Fig. 12, the role of Pb has yet been addressed. After 24 h of exposure to $PbCl_2$, it was confirmed that the original $PbCl_2$ particles had completely transformed to PbO, which was observed on top of the oxide scale. Besides being oxidized to PbO, Pb was also detected in the outer part of the outward growing oxide scale, together with Fe and O according to the cross-sectional SEM/EDX analysis (see Fig. 8 and 9).

Considering these results, an approach was undertaken to isolate the effect of Pb on the corrosion rate, excluding the influence of Cl while maintaining a relevant environment, by exposing T22 in the presence of PbO(s). From these results it was shown that the presence of PbO on the sample surface significantly reduces the oxide growth rate compared to the $PbCl_2$ exposed samples (Fig. 2). Furthermore, exposure in the presence of PbO resulted in the formation of a thinner oxide scale compared to the reference exposures. By comparing the microstructure of the PbO and $PbCl_2$ exposed samples, some differences and similarities can be seen. The top layer of the oxide scale appears similar consisting of Pb, Fe and O and with a similar Pb/Fe ratio. According to the XRD analysis on the samples exposed to PbO, this layer is suggested to consist of Magnetoplumbite ($PbFe_{12}O_{19}$). This composition is further strengthened by EDX analyzes, for both $PbCl_2$ and PbO exposed samples, which detect about 3 - 4 at% Pb (or around 7 - 9 at% based solely on cations, i.e., excluding the oxygen signal). Beyond this layer, the similarities between PbO and $PbCl_2$ exposed samples stops. In the presence of $PbCl_2$, the corrosion attack is rapid, leading to a multilayered oxide scale (as described in the previous section) whereas the presence of PbO leads to a dense, well-adherent and homogenous oxide scale like the reference case. Thus, it seems that corrosion acceleration of $PbCl_2$ is primarily driven by chlorine, rather than Pb.

The presence of PbO appears to promote the formation of $PbFe_{12}O_{19}$ at the oxide scale surface (Figs. 5 and 10) while supressing the formation of hematite as confirmed by XRD and SEM imaging. Beneath the magnetoplumbite layer the partial pressure of oxygen is argued to be below the dissociation pressure of hematite, thus leading to the formation of magnetite and an inward growing mixed spinel as supported by the results from the XRD analysis (Fig. 6). Despite the lack of hematite, which is considered to be the most protective of the iron oxides formed [45] the oxide scale thickness was considerably thinner for the PbO
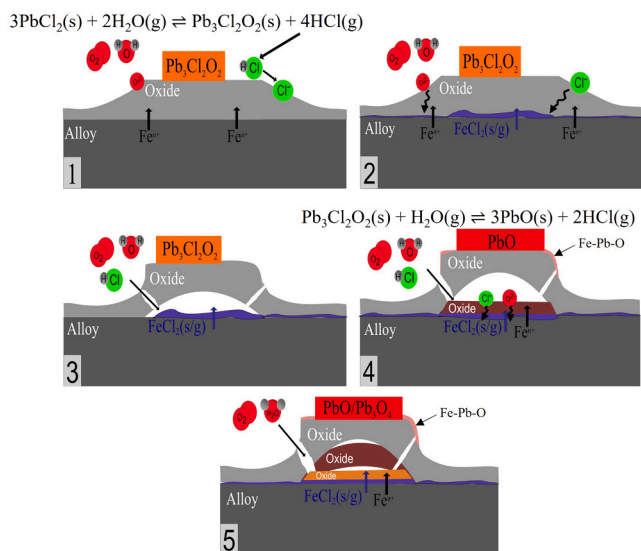
exposed sample compared to the reference exposed sample (Fig. 10). Thus, the results show that the presence of $PbFe_{12}O_{19}$, instead of hematite, reduced the oxide growth which suggests that this oxide phase exhibits good protective properties in this environment. The parabolic-like growth rate together with microstructure analysis strongly indicates that the growth rate is diffusion controlled and as such it appears that the $PbFe_{12}O_{19}$ oxide scale reduces the flux of ions through the oxide scale.

The formation of PbO to $PbFe_{12}O_{19}$ when exposed to $PbCl_2$ is argued to have minimal impact on the corrosion rate on T22. This is attributed to the significant crack formation associated with $FeCl_2$ formation, which is considered to be a pivotal step governing the corrosion rate. The presence of hematite on these samples is proposed to be originating from the secondary oxide scales formed after initial cracking of the primary oxide scale or in surface regions exhibiting low concentration of deposited $PbCl_2$. However, to definitively validate the origin of the hematite peaks observed in XRD, further investigation using more advanced analytical methods such as TEM is required.

In summary, the presence of Pb in $PbCl_2$ does not appear to possess any corrosion-accelerating properties when exposed to T22 at 400 °C in a humid environment. Instead, the corrosive nature of $PbCl_2$ is proposed to be primarily attributed to Cl.

5.2.3. Melt formation

Lastly, a brief discussion on potential melt-induced corrosion is presented. As mentioned in the introduction, $PbCl_2$-induced corrosion has been correlated to the formation of melts that significantly enhance the corrosion rate of various steel types [14,22,30]. Based on previous studies, the current experimental set-up presents two potential sources of melt formation: either from pure $PbCl_2$ or the formation of a low melting eutectic mixture by the $PbCl_2$-$FeCl_2$ system [29]. Since the exposure temperature was deliberately maintained well below the melting point of $PbCl_2$ (501 °C) [22], the melt induced corrosion mechanism of pure $PbCl_2$ initially proposed by [22] can be disregarded. Furthermore, the eutectic melting temperature of the $PbCl_2$-$FeCl_2$ mixture have been reported in literature to vary between 420 - 450 °C and is therefore also disregarded in this study [29,46]. Regrettably, the potential melt mixture of $Pb_3Cl_2O_2$-$FeCl_2$ could not be confirmed as no thermodynamic data base was found for this system. Nevertheless, the microstructural analysis of the corrosion products presented in this study suggests minimal lateral spread of the $PbCl_2$ particles across the sample surface. Based on these observations it is proposed that no melt formation occurred in this study.

6. Conclusions

The presence of $PbCl_2(s)$ strongly accelerates the corrosion attack of the low-alloyed steel T22 at 400 °C in a humid environment. The attack is direct and apparent after 1 h. The resulting corrosion product layer consists of thick oxide scales that are extensively delaminated in connection to the deposited $PbCl_2$ particles.

- The ex-situ deposited $PbCl_2(s)$ is within 1 h converted into Mendipite ($Pb_3Cl_2O_2(s)$) and after 24 h further reacted to PbO(s). These reactions lead to the release of HCl(g), locally, close to the sample surface.
- The released HCl(g) is argued to accelerate the corrosion attack according to electrochemical mechanism, having inward diffusion of chlorine ions and subsequently the formation of $FeCl_2$ at the metal/oxide interface. The presence of $FeCl_2$ is argued to facilitate oxide scale delamination, buckling and subsequently cracking. Through the crack, the gas atmosphere reaches the underlying metal, forming a new oxide scale. The role of Cl in $PbCl_2$-indcued corrosion of low-alloyed steels is argued to be major driving force, through the delamination and cracking process.

- The role of Pb in the corrosion attack is minor. PbO is reacting with iron oxide to form Magnetoplumbite ($PbFe_{12}O_{19}$) as a top layer of the oxide scale which leads to a decreased corrosion rate. The results indicate that Magnetoplumbite offers a better corrosion protection than hematite (Fe_2O_3) at 400 °C for low-alloyed steels, at least up to 168 h.

CRediT authorship contribution statement

Jesper Liske: Writing – review & editing, Supervision, Conceptualization. **Torbjörn Jonsson:** Writing – review & editing, Supervision, Conceptualization. **Hampus Lindmark:** Writing – review & editing, Writing – original draft, Visualization, Investigation, Data curation, Conceptualization.

Declaration of Competing Interest

The authors declare the following financial interests/personal relationships which may be considered as potential competing interests: Hampus Lindmark reports financial support was provided by Chalmers University of Technology. If there are other authors, they declare that they have no known competing financial interests or personal relationships that could have appeared to influence the work reported in this paper.

Data availability

Data will be made available on request.

References

[1] J. Malinauskaite, H. Jouhara, D. Czajczyńska, P. Stanchev, E. Katsou, P. Rostkowski, R.J. Thorne, J. Colon, S. Ponsá, F. Al-Mansour, Municipal solid waste management and waste-to-energy in the context of a circular economy and energy recycling in Europe, Energy 141 (2017) 2013–2044.

[2] A. Kumar, S.R. Samadder, A review on technological options of waste to energy for effective management of municipal solid waste, Waste Manag. 69 (2017) 407–422.

[3] M. Quader, S. Ahmed, Bioenergy with carbon capture and storage (BECCS): future prospects of carbon-negative technologies. Clean Energy for Sustainable Development, Elsevier, 2017, pp. 91–140.

[4] J. Pettersson, Alkali Induced High Temperature Corrosion of Stainless Steel-Experiences from Laboratory and Field, Chalmers University of Technology, 2008.

[5] J. Krook, A. Mårtensson, M. Eklund, Sources of heavy metal contamination in Swedish wood waste used for combustion, Waste Manag. 26 (2006) 158–166.

[6] Y. Alipour, P. Henderson, Corrosion of furnace wall materials in waste-wood fired power plant, Corros. Eng. Sci. Technol. 50 (2015) 355–363.

[7] H. Kinnunen, M. Hedman, M. Engblom, D. Lindberg, M. Uusitalo, S. Enestam, P. Yrjas, The influence of flue gas temperature on lead chloride induced high temperature corrosion, Fuel 196 (2017) 241–251.

[8] D. Bankiewicz, P. Vainikka, D. Lindberg, A. Frantsi, J. Silvennoinen, P. Yrjas, M. Hupa, High temperature corrosion of boiler waterwalls induced by chlorides and bromides–Part 2: lab-scale corrosion tests and thermodynamic equilibrium modeling of ash and gaseous species, Fuel 94 (2012) 240–250.

[9] S. Enestam, R. Backman, K. Mäkelä, M. Hupa, Evaluation of the condensation behavior of lead and zinc in BFB combustion of recovered waste wood, Fuel Process. Technol. 105 (2013) 161–169.

[10] S.H. Enestam, M.K. Fabritius, S.K. Hulkkonen, J.T. Röppänen, Control of ash-related operational problems in BFB combustion of biofuels and waste, Int. Conf. Fluid. Bed Combust. (2003) 541–546.

[11] R.A. Antunes, M.C.L. de Oliveira, Corrosion in biomass combustion: a materials selection analysis and its interaction with corrosion mechanisms and mitigation strategies, Corros. Sci. 76 (2013) 6–26.

[12] J. Niemi, H. Kinnunen, D. Lindberg, S. Enestam, Interactions of PbCl2 with alkali salts in ash deposits and effects on boiler corrosion, Energy Fuels 32 (2018) 8519–8529.

[13] J. Lehmusto, B.-J. Skrifvars, P. Yrjas, M. Hupa, High temperature oxidation of metallic chromium exposed to eight different metal chlorides, Corros. Sci. 53 (2011) 3315–3323.

[14] M. Sánchez Pastén, M. Spiegel, High temperature corrosion of metallic materials in simulated waste incineration environments at 300–600° C, Mater. Corros. 57 (2006) 192–195.

[15] E. Sadeghimeresht, L. Reddy, T. Hussain, N. Markocsan, S. Joshi, Chlorine-induced high temperature corrosion of HVAF-sprayed Ni-based alumina and chromia forming coatings, Corros. Sci. 132 (2018) 170–184.

[16] M. Bøjer, P.A. Jensen, K. Dam-Johansen, O.H. Madsen, K. Lundtorp, Release of corrosive species above the grate in a waste boiler and the implication for improved electrical efficiency, Energy Fuels 24 (2010) 5696–5707.

[17] M.A. Olivas-Ogaz, J. Eklund, A. Persdotter, M. Sattari, J. Liske, J.-E. Svensson, T. Jonsson, The influence of oxide-scale microstructure on KCl (s)-induced corrosion of low-alloyed steel at 400C, Oxid. Met. 91 (2019) 291–310.

[18] E. Larsson, The Corrosive Effect of Chlorine Containing Species on Waterwalls and Superheater Materials in Waste and Biomass-Fired Power Plants, Chalmers Tekniska Hogskola (Sweden), 2017.

[19] A. Talus, R. Norling, L. Wickström, A. Hjörnhede, Effect of lead content in used wood fuel on furnace wall corrosion of 16Mo3, 304L and alloy 625, Oxid. Met. 87 (2017) 813–824.

[20] Y. Alipour, P. Henderson, P. Szakalos, The effect of a nickel alloy coating on the corrosion of furnace wall tubes in a waste wood fired power plant, Mater. Corros. 65 (2014) 217–225.

[21] T. Brunner, J. Fluch, I. Obernberger, R. Warnecke, Investigations of aerosol formation pathways during MSW combustion based on high-temperature impactor measurements, Fuel Process. Technol. 105 (2013) 154–160.

[22] M. Spiegel, Salt melt induced corrosion of metallic materials in waste incineration plants, Mater. Corros. 50 (1999) 373–393.

[23] M. Bøjer, P.A. Jensen, F. Frandsen, K. Dam-Johansen, O.H. Madsen, K. Lundtorp, Alkali/Chloride release during refuse incineration on a grate: full-scale experimental findings, Fuel Process. Technol. 89 (2008) 528–539.

[24] M.W. Chase, N.I.S. Organization, NIST-JANAF Thermochemical Tables, American Chemical Society Washington, DC, 1998.

[25] M. McNallan, W. Liang, S. Kim, C. Kang, Acceleration of the high temperature oxidation of metals by chlorine, high temperature corrosion, NACE (1983) 316.

[26] H. Grabke, E. Reese, M. Spiegel, The effects of chlorides, hydrogen chloride, and sulfur dioxide in the oxidation of steels below deposits, Corros. Sci. 37 (1995) 1023–1043.

[27] D. Bankiewicz, S. Enestam, P. Yrjas, M. Hupa, Experimental studies of Zn and Pb induced high temperature corrosion of two commercial boiler steels, Fuel Process. Technol. 105 (2013) 89–97.

[28] D. Bankiewicz, P. Yrjas, D. Lindberg, M. Hupa, Determination of the corrosivity of Pb-containing salt mixtures, Corros. Sci. 66 (2013) 225–232.

[29] E. Larsson, H. Gruber, K. Hellström, T. Jonsson, J. Liske, J.-E. Svensson, A comparative study of the initial corrosion of KCl and PbCl 2 on a low-alloyed steel, Oxid. Met. 87 (2017) 779–787.

[30] A.M. Núñez, E. Börjesson, H. Kinnunen, D. Lindberg, R. Norling, Influence of PbCl2 and KCl salt mixture on high temperature corrosion of alloy 625, Fuel 358 (2024) 130196.

[31] A. Persdotter, M. Sattari, E. Larsson, M.O. Ogaz, J. Liske, T. Jonsson, Oxidation of Fe-2.25 Cr-1Mo in presence of KCl (s) at 400C–Crack formation and its influence on oxidation kinetics, Corros. Sci. 163 (2020) 108234.

[32] N. Folkeson, T. Jonsson, M. Halvarsson, L.G. Johansson, J.E. Svensson, The influence of small amounts of KCl (s) on the high temperature corrosion of a Fe-2.25 Cr-1Mo steel at 400 and 500° C, Mater. Corros. 62 (2011) 606–615.

[33] C. Schlereth, M.C. Galetz, Effect of total pressure and furnace tube material on the oxidation of T22 in humidified air, Oxid. Met. 96 (2021) 3–15.

[34] T. Jonsson, N. Folkeson, J.-E. Svensson, L.-G. Johansson, M. Halvarsson, An ESEM in situ investigation of initial stages of the KCl induced high temperature corrosion of a Fe–2.25 Cr–1Mo steel at 400C, Corros. Sci. 53 (2011) 2233–2246.

[35] B. Pujilaksono, T. Jonsson, M. Halvarsson, J.-E. Svensson, L.-G. Johansson, Oxidation of iron at 400–600C in dry and wet O2, Corros. Sci. 52 (2010) 1560–1569.

[36] A. Dalvi, D. Coates, A review of the diffusion path concept and its application to the high-temperature oxidation of binary alloys, Oxid. Met. 5 (1972) 113–135.

[37] J. Töpfer, S. Aggarwal, R. Dieckmann, Point defects and cation tracer diffusion in (CrxFe1− x) 3− δO4 spinels, Solid State Ion. 81 (1995) 251–266.

[38] M. Spiegel, A. Zahs, H. Grabke, Fundamental aspects of chlorine induced corrosion in power plants, Mater. High Temp. 20 (2003) 153–159.

[39] A. Zahs, M. Spiegel, H.J. Grabke, Chloridation and oxidation of iron, chromium, nickel and their alloys in chloridizing and oxidizing atmospheres at 400–700C, Corros. Sci. 42 (2000) 1093–1122.

[40] M. Uusitalo, P. Vuoristo, T. Mäntylä, High temperature corrosion of coatings and boiler steels below chlorine-containing salt deposits, Corros. Sci. 46 (2004) 1311–1331.

[41] P. Viklund, R. Pettersson, HCl-induced high temperature corrosion of stainless steels in thermal cycling conditions and the effect of preoxidation, Oxid. Met. 76 (2011) 111–126.

[42] N. Folkeson, L.-G. Johansson, J.-E. Svensson, Initial stages of the HCl-induced high-temperature corrosion of alloy 310, J. Electrochem. Soc. 154 (2007) C515.

[43] A. Zahs, M. Spiegel, H. Grabke, The influence of alloying elements on the chlorine-induced high temperature corrosion of Fe-Cr alloys in oxidizing atmospheres, Mater. Corros. 50 (1999) 561–578.

[44] P. Viklund, A. Hjörnhede, P. Henderson, A. Stålenheim, R. Pettersson, Corrosion of superheater materials in a waste-to-energy plant, Fuel Process. Technol. 105 (2013) 106–112.

[45] P. KOFSTAD. High Temperature Corrosion 568, Elsevier Applied Science, London and New York, 1988.

[46] W.-G. Seo, H. Matsuura, F. Tsukihashi, Calculation of phase diagrams for the FeCl 2, PbCl 2, and ZnCl 2 binary systems by using molecular dynamics simulation, Metall. Mater. Trans. B 37 (2006) 239–251.